Photoelectron momentum distributions of the hydrogen atom driven by multicycle elliptically polarized laser pulses

Mitsuko Murakami and Shih-I Chu

Photoelectron Momentum Distributions of the Hydrogen Atom Driven by Multi-cycle Elliptically Polarized Laser ~~Fields~~ Pulses

Mitsuko Murakami[1, *] and Shih-I Chu[1, 2]

[1]*Center for Quantum Science and Engineering,*

and Center for Advanced Study in Theoretical Sciences,

Department of Physics, National Taiwan University, Taipei 10617, Taiwan

[2]*Department of Chemistry, University of Kansas, Lawrence, Kansas 66045, USA*

Abstract

Photoelectron momentum distributions (PMDs) of the hydrogen atom driven by multi-cycle, elliptically polarized strong laser fields are studied in detail, based on the numerical solution of the time-dependent Schrödinger equation and the Volkov wave propagation. Both short and long driving pulses of 800nm field are considered, as well as the ellipticity dependence, to describe the mechanism of symmetry breaking in the hydrogen atom PMD. Moreover, we demonstrate that ~~the amount of retardation angles~~ the value of a retardation angle in the longitudinal PMD can depend on the order of above-threshold ionization spectra.

---
* mitsuko@phys.ntu.edu.tw

I.   INTRODUCTION

The photoelectron momentum spectroscopy of atoms using an elliptically polarized laser field provides both temporal and structural information about ionizing electrons with unprecedented accuracies. In the last decade, detailed measurements of rare-gas atoms were conducted for both longitudinal [1–4] and transversal [5, 6] photoelectron momentum distributions (PMDs).

Experimentally observed PMDs exhibit some features which are in conflict with traditional theories. For instance, the Ammosov-Delone-Krainov tunneling model tends to underestimate the transversal width of a PMD by 15% [5]; the location of a peak in the longitudinal PMD does not align with the minor axis of a polarization ellipse as the strong field approximation (SFA) predicts [1, 7]. These discrepancies were attributed in the past to effects of ionic potentials, tunnelling delay time, dynamical Stark shifts, coulomb focusing, or induced polarizations; see Ref. [8] and references therein. Theoretical calculations of PMDs based on the time-dependent Schrödinger equation (TDSE) [7, 9–11] or the nonadiabatic SFA [2, 12, 13] confirmed some of the findings of those experiments, but further investigations are needed to address additional questions, such as the role of inner electrons and the dependence on atomic species [14–17].

Recently, a detailed comparison between the TDSE and the nonadiabatic SFA calculations of the longitudinal PMD was made for the hydrogen atom, using 800nm, few-cycle driving lasers of various peak intensities [18]. Its authors argued that the hydrogen atom PMD can be used as a reference to identify the multi-electron effect in the ~~amount of retardation angles~~ value of retardation angle measured in attoclock experiments [1–3]. Moreover, the ellipticity dependence on the transversal width of the PMD driven by a few-cycle laser pulse was studied in Ref. [11] based on the TDSE of the hydrogen atom. The measurement of hydrogen PMD has been realized only recently [19], raising the importance of accurate calculations of the hydrogen atom as never before. In this work, we complement their study of the hydrogen atom PMD using multi-cycle driving laser pulses (> 5 optical cycles). The multi-cycle driving laser is useful in resolving above-threshold ionization spectra for each number of photons absorbed. Combined with an XUV pulse train, it can probe subcycle dynamics of electrons in a stroboscopic manner [20]. Effects of various laser parameters are discussed, such as carrier envelope phase (CEP) and ellipticity, using the 800nm driving

laser field of the peak intensity 5×10^{13} W/cm². A particular emphasis is placed on the study of symmetry breaking in the non-adiabatic regime. The calculation is based on the generalized pseudospectral (GPS) method for the inner region [21] and the propagation under the Volkov Hamiltonian in the momentum space for the outer region [22, 23]. The PMD of the hydrogen atom driven by a multi-cycle, linearly-polarized driving laser field has been studied in detail based on the GPS method in Refs. [24] and [25] in the past. Our work extends them for elliptically-polarized driving laser fields.

The paper is organized as follows. In Sec. II, numerical methods to calculate the PMD of the hydrogen atom in an elliptically-polarized laser field are described. Results are presented in Sec. III. First, we describe the property of the hydrogen atom PMD driven by a long (20 cycle), circularly-polarized laser field in Sec. III A 1. The effect of ellipticity on the PMD is studied in Sec. III A 2. We will find that the amount of ~~retardation angles~~ a retardation angle in the longitudinal PMD can depend on the order of above-threshold ionization spectra. Next, the symmetry breaking in the PMD and the effect of CEP associated with a shorter driving laser (6 cycle) ~~is~~ are discussed in Sec. III B 1 and Sec. III B 2, respectively. Finally, Concluding remarks are given in Sec. IV. Atomic units ($e = m_e = \hbar = 1$) are used throughout, unless specified otherwise.

II. METHODS

We solve the TDSE in the length gauge:

$$i\frac{\partial}{\partial t}\psi(\mathbf{r}, t) = [\mathcal{H}_0 + V(\mathbf{r}, t)]\psi(\mathbf{r}, t).\tag{1}$$

The stationary Hamiltonian $\mathcal{H}_0$ of the hydrogen atom for the GPS method is given in Ref. [21]. The laser-atom interaction potential in the limit of dipole approximation is $V(\mathbf{r}, t) = \mathbf{E}(t) \cdot \mathbf{r}$. We define an elliptically-polarized driving laser field of frequency ω_o as [3]

$$\mathbf{E}(t) = E_o(t) \left[\frac{1}{\sqrt{\varepsilon^2 + 1}} \cos(\omega_o t + \alpha) \, \hat{\mathbf{z}} + \frac{\varepsilon}{\sqrt{\varepsilon^2 + 1}} \sin(\omega_o t + \alpha) \, \hat{\mathbf{x}} \right],\tag{2}$$

where ε is an ellipticity constant, α is a CEP, and $E_o(t)$ is a pulse envelope function centered around $t = 0$, given by

$$E_o(t) = \sqrt{I_o} \cos^2\left(\frac{\omega_o t}{2n}\right),\tag{3}$$

with I_o and n being the peak intensity for $\varepsilon = 0$ and the number of optical cycles ($T = 2\pi/\omega_o$) per pulse, respectively. In the spherical coordinates, the interaction potential is therefore

$$V(\mathbf{r}, t) = E_o(t)r \left[\frac{1}{\sqrt{\varepsilon^2 + 1}} \cos\theta \cos(\omega_o t + \alpha) + \frac{\varepsilon}{\sqrt{\varepsilon^2 + 1}} \sin\theta \cos\phi \sin(\omega_o t + \alpha) \right]. \qquad (4)$$

Unless in a linearly-polarized field ($\varepsilon = 0$), the azimuthal symmetry of the total Hamiltonian is broken, and therefore the fully three-dimensional TDSE is solved by using the GPS method [26]. That is, we expand the solution in terms of the spherical harmonics $Y_{\ell m}$ as

$$\psi(\mathbf{r}, t) = \sum_{\ell,m} \frac{R_{\ell m}(r, t)}{r} Y_{\ell m}(\theta, \phi), \qquad (5)$$

and evolve the following radial wavefunction mapped onto the Legendre-Lobatto collocation points $\{x_j\} \in [-1, 1]$.

$$\varphi_{\ell m}(x_j, t) = R_{\ell m}(r(x_j), t) \frac{\sqrt{r'(x_j)}}{P_N(x_j)} \sqrt{\frac{2}{N(N+1)}} \quad (j = 1, 2, \cdots, N - 1), \qquad (6)$$

where $P_N(x_j)$ is the Nth-order Legendre polynomial, and

$$\left\{ x_j : (1 - x_j{}^2) P_N{}'(x_j) = 0 \right\} \quad (j = 0, 1, 2, \cdots, N). \qquad (7)$$

Its normalization condition (without the presence of absorbing boundaries) is simply

$$\sum_{\ell,m,j} |\varphi_{\ell m}(x_j, t)|^2 = 1. \qquad (8)$$

Angular coordinates on the polarization plane are discretized regularly and mapped onto a set of Legendre-Gauss collocation points $\{y_\lambda\} \in [-1, 1]$ as follows.

$$\theta_\lambda = \frac{\pi \lambda}{N_\ell} \quad (\lambda = 0, 1, 2, \cdots, N_\ell), \qquad (9)$$

where $y_\lambda \equiv \cos\theta_\lambda$ are the roots of Legendre polynomials:

$$\{y_\lambda : P_{N_\ell + 1}(y_\lambda) = 0\}. \qquad (10)$$

Azimuthal angles around the major polarization axis are discretized regularly as

$$\phi_\mu = \frac{2\pi \mu}{2N_\ell + 1} \quad (\mu = 0, 1, 2, \cdots, 2N_\ell). \qquad (11)$$

To eliminate reflections from the boundary in the configuration space, we split the wave function at a given time t as [22, 23]

$$\psi(\mathbf{r}, t) = f(r)\psi(\mathbf{r}, t) + [1 - f(r)]\psi(\mathbf{r}, t) = \psi_{\text{(in)}}(\mathbf{r}, t) + \psi_{\text{(out)}}(\mathbf{r}, t), \qquad (12)$$

4

where $f(r)$ is an absorbing function that is one in the inner region ($0 \le r \le R_b$) and smoothly decreases to zero in the outer region ($R_b < r < r_{\max}$). In our calculations, R_b is set at five times the classical oscillator radius ($= \sqrt{I_o}/\omega_o{}^2$), whereas $r_{\max}$ is set either at ten times the classical oscillator radius or at 100 au, whichever is larger. For the evaluation of photoelectron spectra in particular, only the outer wave function is necessary, and it is propagated in the momentum space under the Volkov Hamiltonian in the velocity gauge [22]. That is, in each time step, we calculate ~~the~~ the Fourier transform of the outer wave function:

$$\tilde{\psi}^{\mathrm{v}}_{(\mathrm{out})}(\mathbf{p}, t) = \iiint d^3r \, \frac{e^{-i[\mathbf{p}+\mathbf{A}(t)]\cdot\mathbf{r}}}{(2\pi)^{3/2}} \psi_{(\mathrm{out})}(\mathbf{r}, t), \tag{13}$$

where $\mathbf{A}(t) = -\int_{-\infty}^{t} \mathbf{E}(t')dt'$ is the vector potential, and the superscript v in $\tilde{\psi}^{\mathrm{v}}_{(\mathrm{out})}$ denotes the velocity gauge. Coordinates in the momentum space are regularly discretized as

$$p_j = j\Delta p \quad (j = 1, 2, \cdots, N_p). \tag{14}$$

The angular coordinates (θ_p, ϕ_p) of the outer wave function in the momentum space are discretized in the same manner as (θ, ϕ) in the configuration space. For results presented in this work (800nm, $I_o = 5 \times 10^{13}$ W/cm^2), the number of collocation points used are N=250 and N_ℓ=64, whereas the spacing for $\{p_j\}$ is $\Delta p = 0.005$, and the time step is $\Delta t = 0.2$. The number of collocation points in the configuration space we chose ensures the convergence of ionization probability during the time evolution. The fine spacing for Δp was necessary for the high-resolution presentation of PMDs, though the Volkov-wave propagation is stable with lesser number of points in $\{p_j\}$.

Using the spherical-wave expansion:

$$\frac{e^{-i\mathbf{p}\cdot\mathbf{r}}}{(2\pi)^{3/2}} \sim \sqrt{\frac{2}{\pi}} \sum_{\ell,m} (-i)^\ell \mathcal{J}_\ell(pr) Y^*_{\ell m}(\theta, \phi) Y_{\ell m}(\theta_p, \phi_p), \tag{15}$$

where $\mathcal{J}_\ell$ are the spherical Bessel functions, and (p, θ_p, ϕ_p) are the coordinates in the momentum space, Eq. (13) becomes

$$\tilde{\psi}^{\mathrm{v}}_{(\mathrm{out})}(p_j, \theta_\lambda, \phi_\mu, t) = \sqrt{\frac{2}{\pi}} \mathcal{S} \left\{ (-i)^\ell \sum_j r(x_j) \sqrt{w_j r'(x_j)} \varphi^{\mathrm{v}}_{\ell m \, (\mathrm{out})}(x_j, t) \mathcal{J}_\ell(p_j r(x_j)) \right\} (\theta_\lambda, \phi_\mu), \tag{16}$$

where $\mathcal{S} : (\ell, m) \to (\theta_\lambda, \phi_\mu)$ is the spherical harmonic transform [27]:

$$\mathcal{S}\{\varphi_{\ell m}(x_j, t)\}(\theta_\lambda, \phi_\mu) \equiv \sum_{\ell,m} Y_{\ell m}(\theta_\lambda, \phi_\mu) \varphi_{\ell m}(x_j, t)$$
$$= \varphi(x_j, \theta_\lambda, \phi_\mu, t), \tag{17}$$

and $\{w_j\}$ are the quadrature weights for the Legendre-Lobatto collocation points $\{x_j\}$:

$$w_j = \frac{2}{N(N+1)} \frac{1}{[P_N(x_j)]^2}. \tag{18}$$

The velocity-gauge wave function in Eq. (16) is given by

$$\varphi^{\mathrm{v}}_{\ell m \, (\mathrm{out})}(x_j, t) = \mathcal{S}^{-1} \left\{ e^{-i\mathbf{A}(t)\cdot\mathbf{r}} \mathcal{S} \left\{ \varphi_{\ell m \, (\mathrm{out})}(x_j, t) \right\} (\theta_\lambda, \phi_\mu) \right\} (\ell, m), \tag{19}$$

where $\mathcal{S}^{-1} : (\theta_\lambda, \phi_\mu) \to (\ell, m)$ is the inverse spherical harmonic transform.

Eq. (16) is added to the wave function ψ^{v}_∞ in the momentum space (where the subscript ∞ indicates that it is at a very large distance from the nucleus so that the binding potential can be ignored) and evolved with the Volkov Hamiltonian in the velocity gauge:

$$\mathcal{H}^{\mathrm{v}}_\infty(t) = \frac{[\mathbf{p} + \mathbf{A}(t)]^2}{2}, \tag{20}$$

such that

$$\psi^{\mathrm{v}}_\infty(p_j, \theta_\lambda, \phi_\mu, t + \Delta t) = e^{-i\mathcal{H}^{\mathrm{v}}_\infty(t)\Delta t} \left[\psi^{\mathrm{v}}_\infty(p_j, \theta_\lambda, \phi_\mu, t) + \tilde{\psi}^{\mathrm{v}}_{(\mathrm{out})}(p_j, \theta_\lambda, \phi_\mu, t) \right], \tag{21}$$

with an initial condition: $\psi^{\mathrm{v}}_\infty(p_j, \theta_\lambda, \phi_\mu, t_0) = 0$.

The PMD is evaluated from the outer state in the end of the time evolution ($t = t_f$) as

$$D(p_j, \theta_\lambda, \phi_\mu) = |\psi^{\mathrm{v}}_\infty(p_j, \theta_\lambda, \phi_\mu, t_f)|^2. \tag{22}$$

For calculations using short ($n = 6$ cycle) driving laser fields, the time evolution is continued for two empty optical cycles after the end of the pulse to allow some time for relaxations.

III.   RESULTS

A.   PMD in the Adiabatic Regime

1.   Circular polarization

Figure 1 shows the PMD of the hydrogen atom, driven by a long ($n = 20$ cycle), circularly-polarized ($\varepsilon = 1$) 800nm laser field of peak intensity $I_o = 5 \times 10^{13}$ W/cm^2. The CEP of Eq. (2) is set as $\alpha = \pi/2$, which makes the field strength $\mathbf{E}(t)$ to maximize in the positive x-direction at the pulse peak ($t = 0$); there are two equally strong field maxima in the opposite

6

directions of the z-axis before and after the pulse peak, but their strength would be slightly weaker than $\sqrt{I_o/2}$ because of the CEP. The effect of CEP becomes important only with shorter and stronger driving laser pulses, as we discuss in Section III B 2. With a 20-cycle driving laser used for FIG. 1, the adiabatic approximation holds, i.e., subcycle modulations in the field strength are averaged out. For a circularly polarized field in particular, the kinetic energy of the electron on the polarization plane under the adiabatic approximation is independent of the direction θ_p of momentum vectors and given by [28]

$$p^2/2 = s\,\omega_o + n_o\,\omega_o - I_p - U_p \quad (s = 0, 1, 2, \cdots), \tag{23}$$

where s is the number of above-threshold photons absorbed, I_p is the ionization potential, $U_p = I_o/4\omega_o{}^2$ is the ponderomotive energy, and

$$n_o = \lfloor I_p/\omega_o \rfloor + 1. \tag{24}$$

For the 800nm, $I_o = 5 \times 10^{13}$ W/cm^2 driving laser we use, $U_p = 2.994$ eV, $\omega_o = 1.55$ eV, and $n_o = 9$ for the hydrogen atom ($I_p = 13.6$ eV).

FIG. 1(a) shows the longitudinal PMD, i.e., the cross section on the polarization plane ($p_y = 0$). In the adiabatic limit, the hydrogen atom PMD can be calculated for each s using the S-matrix formalism [28]. In our calculation, all the different channels ($s = 0, 1, 2, \cdots$) contribute to the PMD with different strengths, but they appear separately at a radial distance of

$$p_s = \sqrt{2(s\,\omega_o + n_o\,\omega_o - I_p - U_p)}. \tag{25}$$

FIG. 1(b) is the transversal PMD, i.e., the cross section on the plane perpendicular to the polarization vectors ($p_z = 0$). The SFA prediction for the transversal width of the hydrogen atom PMD driven by a few-cycle laser is given in Ref. [12]. Their work also provides the TDSE calculation for the hydrogen atom using a half-cycle linearly polarized driving laser. The half-cycle linearly polarized laser is known to induce the same transversal width as a few-cycle circularly polarized laser in the PMD of the soft-Coulomb potential [9]. The PMD in the adiabatic regime, however, is split into many layers depending on the number of above-threshold photons absorbed, as shown in FIG. 1(b). In Figure 2, we plot the transversal PMD of FIG. 1(b) along the radius p_s given by Eq. (25) as a function of angle ϕ_p, defined counter-clockwise from the positive p_x-axis. For a comparison, their density is normalized between $\phi_p = 90$ and 270 degrees. We find that the distribution becomes narrower as the number

of absorbed photons increases. The measurement of transversal PMD in Ref. [5, 6] did not distinguish each layer at p_s, whereas the time-resolved measurement using an attosecond pulse train [20] or a two-color (XUV + near infared) free-electron laser [29–31] ~~probably would~~ could.

In FIG. 1(c), we re-plot the transversal PMD of FIG. 1(a) as a function of angle θ_p, defined counter-clockwise from the positive p_z-axis, and of the kinetic energy $(|p_z|^2 + |p_x|^2)/2$, on the polarization plane. Eq. (23) predicts that the electron has negative kinetic energy when $s \leq 1$; they are classically forbidden transitions. FIG. 1(c) shows a faint but clear transition line at 0.456 eV, which corresponds to the kinetic energy of the $s = 2$ transition. To clarify the location of the spectral peaks, we plot the above threshold ionization (ATI) spectra in Figure 3, which is obtained by integrating θ_p out of FIG. 1(c). The spectral strength peaks at $s = 5$ and steadily falls beyond, consistent to he cutoff predicted by SFA; i.e., $2U_p = 5.988$ eV.

There is a striking difference between the ATI spectra of the hydrogen atom driven by a circularly-polarized field in FIG. 3 and the ones generated by linearly-polarized fields. That is, the lowest ATI peaks ($s = 2, 3$) in FIG. 3 show very low intensity in comparison to the other peaks around the cutoff ($s = 4, 5, 6$), whereas the ATI peaks in linearly-polarized fields have a pronounced fundamental peak followed by equally-strong plateau harmonics [24, 25]. We must note that our present calculation employs the Volkov approximation, i.e., the interaction of the electron with the nucleus is neglected during the propagation of outer wave function, which could in principle result in an unphysical behaviour in the low-energy ATI spectra, particularly when a long-wavelength ($> 1\mu m$) driving laser is used [32]. However, the lowest-order ATI peaks were also absent (or have negligibly small intensities) in the experimentally measured PMDs [1–3], using near-infrared ($\sim 800nm$), near-circular ($\varepsilon = 0.87$) driving lasers similar to our calculations. We thus believe the reduced intensity at the lowest-order ATI peaks in FIG. 3 is not an artifact of the Volkov approximation but real. One possible explanation is that, in the case of circular polarization, part of the energy of a tunnelling electron is transferred into the kinetic energy in the transversal direction, decreasing the longitudinal energy to break the binding potential [13]. This would make the intensity at the lowest-order ATI spectra smaller compared to the linear polarization case.

2. Ellipticity Dependence

Figure 4 shows the longitudinal PMD in the 20-cycle driving laser field (800nm, $I_o = 5 \times 10^{13}$ W/cm^2, $\alpha = \pi/2$) for various ellipticity constants ($0 \leq \varepsilon < 1$). In the adiabatic regime, the angular distribution of a hydrogen atom PMD on the polarization plane is known to have a two-fold symmetry [28]; that is,

$$\cancel{D_s(\zeta, \theta_p) = D_s(\zeta, \theta_p + \pi);}$$

$$D_s(p, \theta_p) = D_s(p, \theta_p + \pi), \tag{26}$$

where D_s denotes the ionization probability to a fixed multiphoton channel s ~~, computed at the retardation angle ζ due to the Coulomb potential~~. In FIG. 4, we find that the above symmetry indeed holds true regardless the ellipticity ε.

The ellipticity in a driving field introduces a preferred axis of ionization, which makes the PMD to concentrate along the minor axis of a polarization ellipse (orthogonal to the behaviour in the configuration space) but shifted by a retardation angle. A similar effect is known for the PMD of hydrogen molecular ion (H$_2{}^+$) in a circularly-polarized driving laser field [33]; the preferred axis of ionization in this case is created by the molecular potential itself, i.e., the most electron ionize along the molecular axis.

The retardation angle in a PMD is defined as a deviation of the PMD maximum from the minor axis of a polarization ellipse [7]. A major contribution to the amount of a retardation angle comes from the deflection of electron trajectories due to the Coulomb potential. In a classical approximation, it is given by [34]

$$\xi = \sin^{-1}\left(\frac{1}{\epsilon}\right), \tag{27}$$

where ϵ is an orbital eccentricity:

$$\epsilon = \sqrt{1 + \frac{2L_s{}^2(s\,\omega_o + n_o\,\omega_o - I_p - U_p)}{m_e e^4}}, \tag{28}$$

where $L_s = sh\hbar$ is an angular momentum of an ionized electron, and $h = 2\varepsilon/(\varepsilon^2 + 1)$ is the light helicity of a driving laser field. In particular, $\varepsilon = 0$ (linear polarization) makes $L_s = 0$, and therefore Eq. (27) gives $\xi = \pi/2$; i.e., the PMD concentrates along the major axis of a polarization ellipse, as shown in the inset figure of FIG. 4(a). In reality, the retardation angle

9

also depends on the tunnelling time delay [13], the Wigner time delay [35], the relativistic time delay [36], and other quantum-mechanical effects.

In FIG. 4(a) and (b), the field is either linear ($\varepsilon = 0$) or close to linear ($\varepsilon = 0.2$), and we observe an interference of electron density creating nodes in the PMD along the concentric circle of radius p_s given by Eq. (25). The interference pattern in a PMD signifies the rescattering of an electron with the ionized core [24]. In FIG. 4(c)-(f) where the field is closer to circular ($\varepsilon \geq 0.4$), there is no sign of rescattering, but the PMDs gradually ~~concentrate along the minor axis of the polarization ellipse~~ shift the axis of concentration toward the minor axis of a polarization ellipse ($\theta_p = \pm 90$ degree), as an ellipticity ε of the field increases. This can most clearly be seen in the inset figures, where we plot the radially integrated and normalized electron distributions.

Furthermore in FIG. 4(c)-(f), we find that the lowest-order spectrum ($s = 2$) has much larger retardation angle ~~, i.e., the angle between the minor axis of polarization ellipse and the PMD peak,~~ than the rest ($s > 2$). To elucidate this point, we plot the longitudinal PMDs of FIG. 4 as a function of polar angle θ_p and kinetic energy on the polarization plane in Figure 5. In these figures, one can observe the way PMDs shift their peaks at each p_s ($s = 2, 3, \cdots$) to the negative θ_p direction as an ellipticity of the field increases. In these figures, the retardation angle of the lowest-order ($s = 2$) channel is much larger than the $s = 4$, which is consistent to the S-matrix prediction in Ref. [28]; the ionization mechanism for the $s = 2$ channel should be very different from the rest. We also notice that the lowest-order ionization $s = 2$ becomes less and less significant compared to the higher-order channels as the ellipticity increases, indicating the enhancement of tunnelling from the excited states. The retardation angles measured in the attoclock measurements for various ellipticity [3] were not resolved for the number of photon absorbed, but our calculation suggests that a separate measurement may be needed for each order of ATI spectra to reveal true electron dynamics in an elliptically polarized field. Lastly, the Volkov approximation employed in our calculation should be valid even for low-energy electrons (< 10 eV), as long as the near-infrared driving-laser ($< 1\mu m$) is used [32]. It is nevertheless desirable to complement our study with other theoretical approaches, such as the path-integrals [37] or the Froquet theory [38] in the future.

B. Non-adiabatic Effects

1. Symmetry Breaking

In this section, we demonstrate that the two-fold symmetry of hydrogen atom PMD in Eq. (26) breaks down when the shorter and stronger driving laser pulse is used. Figure 6 shows the PMD of the hydrogen atom driven by a short ($n = 6$ cycle) circularly-polarized driving laser pulse. All the driving laser parameters remain the same as in FIG. 1 except for the driving laser duration. The symmetry breaking of the PMD is most clearly seen in FIG. 6(c), where we plot the longitudinal PMD as s function of angle θ_p and kinetic energy on the polarization plane. Unlike the adiabatic case in FIG. 1(c), the kinetic energy is no longer a constant of θ_p but modulates with the subcycle change in the strengths of the driving laser field; this causes an asymmetry in the PMD. In the classical limit, the electron momentum vector would take a trajectory given by $-\mathbf{A}(t)$, as shown with a solid red line in FIG. 6(a). As we set $\alpha = \pi/2$ in Eq. (2), the classical momentum has its peak in the direction of positive p_z-axis (i.e., $\theta_p = 0$), while the driving field $\mathbf{E}(t)$ has its peak in the direction of positive x-axis. If we radially integrate the longitudinal PMD in FIG. 6(a), then we would find that the electron density is largest at $\theta_p = 0$ and smallest at $\theta_p = 180$ degrees.

Aside from the symmetry breaking, we should also note that the spectral widths of the PMD in FIG. 6 are broader than the adiabatic case in FIG. 1. When a few-cycle driving laser pulse is used, the PMD does not resolve any spectra at all but forms one continuous band concentrated at the peak of $-\mathbf{A}(t)$ but shifted by a retardation angle; see Ref. [18] for such examples. The lowest-order transition at $s = 2$ in FIG. 6(c) is not as strong as in FIG. 1(c) relative to the higher transitions; this would imply the enhancement of tunnelling ionization from the excited states in the non-adiabatic regime, whose energy continuously shifts upwards while passing through potential barriers [13].

2. Effect of CEPs

The effect of a CEP in a circularly polarized field ($\varepsilon = 1$) is simply to shift the modulation of PMD on the polarization plane around the propagation axis [39]. For example, if we let $\alpha = 0$ in FIG. 6, the momentum vector for each s on the polarization plane would maximize at $\theta_p = -90$ degree, rather than at $\theta_p = 0$ for the $\alpha = \pi/2$ case as shown. In a long,

circularly polarized field, phase shifts due to the CEP do not affect the appearance of PMD at all, as shown in FIG. 1. However, with a shorter driving laser, the phase shift has a subtle effect on the PMD when combined with the existence of a preferred axis of ionization.

Figure 7 shows the PMD driven by the 6-cycle, elliptically polarized ($\varepsilon = 0.87$) laser field of two different CEPs: $\alpha = 0$ and $\alpha = \pi/2$. Notice that the longitudinal PMDs in FIG. 7(a) and (d) are localized around $\theta_p \sim \pm 110$ degrees. In general, when $0 \leq \varepsilon < 1$, the longitudinal PMD driven by an elliptically-polarized laser field would concentrate along the minor axis of the polarization ellipse, but ~~slightly~~ shifted by the amount of a retardation angle (Sec. III A 2); this is true regardless of the driving-laser duration or CEPs.

In FIG. 7, the 6-cycle driving laser ~~induced~~ pulse is inducing a modulation in the magnitude of the momentum vector, reflecting the subcycle change in the strengths of a driving laser field, which ~~broke~~ breaks the symmetry relation (26) when $\alpha = 0$ (top row). On the other hand, when $\alpha = \pi/2$ (bottom row), the symmetry is retained (see the inset figure), but very few electron ~~is ionizing~~ are being ionized at the peak of the classical limit $-\mathbf{A}(t)$, because it is not aligned with the minor axis of the polarization ellipse due to the shift by a retardation angle. In the attoclock measurements [1–3], the CEP in an elliptically polarized field has been stabilized to preserve the two-fold symmetry of PMDs.

IV. CONCLUSION

In this paper, we investigated the PMD of hydrogen atom driven by a multi-cycle, elliptically polarized laser field. Both long and short driving laser are considered to exemplify the mechanisms of symmetry breaking in the hydrogen atom PMD. We showed that the electron momentum on the polarization plane appear separately for the number of above-threshold photons absorbed, and modulates its ~~strengths~~ magnitude only in the non-adiabatic regime, reflecting the subcycle change in the strengths of a driving laser pulse. On the other hand, the ellipticity in a driving-laser field creates the preferred axis of ionization regardless of the driving laser duration. As a result, the two-fold symmetry of the PMD breaks down in the non-adiabatic regime unless the CEP is adjusted so that there are two equally strong field maxima along the major axis of the polarization ellipse. In addition, we found that the retardation angle in the longitudinal PMD for the lowest-order ATI ($s = 2$) is much larger than the rest of the spectra ($s > 2$). This suggests that the ionization mechanics can depend

on the orders of the ATI.

---

[1] P. Eckle, A. N. Pfeiffer, C. Cirelli, A. Staudte, R. Dörner, H. G. Muller, M. Büttiker, and U. Keller, Science **322**, 1525 (2008).

[2] A. N. Pfeiffer, C. Cirelli, M. Smolarski, D. Dimitrovski, M. Abu-samha, L. B. Madsen, and U. Keller, Nature Physics **8**, 76 (2011).

[3] A. N. Pfeiffer, C. Cirelli, A. S. Landsman, M. Smolarski, D. Dimitrovski, L. B. Madsen, and U. Keller, Phys. Rev. Lett. **109**, 083002 (2012).

[4] D. Shafir, H. Soifer, C. Vozzi, A. S. Johnson, A. Hartung, Z. Dube, D. M. Villeneuve, P. B. Corkum, N. Dudovich, and A. Staudte, Phys. Rev. Lett. **111**, 023005 (2013).

[5] L. Arissian, C. Smeenk, F. Turner, C. Trallero, A. V. Sokolov, D. M. Villeneuve, A. Staudte, and P. B. Corkum, Phys. Rev. Lett. **105**, 133002 (2010).

[6] C. T. L. Smeenk, L. Arissian, B. Zhou, A. Mysyrowicz, D. M. Villeneuve, A. Staudte, and P. B. Corkum, Phys. Rev. Lett. **106**, 193002 (2011).

[7] C. P. J. Martiny, M. Abu-samha, and L. B. Madsen, J. Phys. B: At. Mol. Opt. Phys. **42**, 161001 (2009).

[8] N. I. Shvetsov-Shilovski, D. Dimitrovski, and L. B. Madsen, Phys. Rev. A **85**, 023428 (2012).

[9] J. Henkel, M. Lein, V. Engel, and I. Dreissigacker, Phys. Rev. A **85**, 021402(R) (2012).

[10] I. A. Ivanov and A. S. Kheifets, Phys. Rev. A **89**, 021402(R) (2014).

[11] I. A. Ivanov, Phys. Rev. A **90**, 013418 (2014).

[12] I. Dreissigacker and M. Lein, Chemical Physics **414**, 69 (2013).

[13] M. Klaiber, K. Z. Hatsagortsyan, and C. H. Keitel, Phys. Rev. Lett. **114**, 083001 (2015).

[14] G. Zhu, M. Schuricke, J. Steinmann, J. Albrecht, J. Ullrich, I. Ben-Itzhak, T. J. M. Zouros, J. Colgan, M. S. Pindzola, and A. Dorn, Phys. Rev. Lett. **103**, 103008 (2009).

[15] A. Fleischer, H. J. Wörner, L. Arissian, L. R. Liu, M. Meckel, A. Rippert, R. Dörner, D. M. Villeneuve, P. B. Corkum, and A. Staudte, Phys. Rev. Lett. **107**, 113003 (2011).

[16] M. Spanner, J. Mikosch, A. Gijsbertsen, A. E. Boguslavskiy, and A. Stolow, New Journal of Physics **13**, 093010 (2011).

[17] M. Schuricke, G. Zhu, J. Steinmann, K. Simeonidis, I. Ivanov, A. Kheifets, A. N. Grum-Grzhimailo, K. Bartschat, A. Dorn, and J. Ullrich, Phys. Rev. A **83**, 023413 (2011).

[18] L. Torlina, F. Morales, J. Kaushal, I. Ivanov, A. Kheifets, A. Zielinski, A. Scrinzi, H. G. Muller, S. Sukiasyan, M. Ivanov, and O. Smirnova, Nature Physics **11**, 503 (2015).

[19] A. S. Stodolna, A. Rouzée, F. Lépine, S. Cohen, F. Robicheaux, A. Gijsbertsen, J. H. Jungmann, C. Bordas, and M. J. J. Vrakking, Phys. Rev. Lett. **110**, 213001 (2013).

[20] J. Mauritsson, P. Johnsson, E. Mansten, M. Swoboda, T. Ruchon, A. L'Huillier, and K. J. Schafer, Phys. Rev. Lett. **100**, 073003 (2008).

[21] X.-M. Tong and S.-I. Chu, Chemical Physics **217**, 119 (1997).

[22] M. Lein, J. P. Marangos, and P. L. Knight, Phys. Rev. A **66**, 051404(R) (2002).

[23] X. M. Tong, K. Hino, and N. Toshima, Phys. Rev. A **74**, 031405(R) (2006).

[24] D. A. Telnov and S.-I. Chu, Phys. Rev. A **79**, 043421 (2009).

[25] Z. Zhou and S.-I. Chu, Phys. Rev. A **83**, 013405 (2011).

[26] M. Murakami, O. Korobkin, and M. Horbatsch, Phys. Rev. A **88**, 063419 (2013).

[27] N. Schaeffer, Geochemistry, Geophysics, Geosystems **14**, 751 (2013).

[28] S. Basile, F. Trombetta, and G. Ferrante, Phys. Rev. Lett. **61**, 2435 (1988).

[29] M. Meyer, P. Radcliffe, T. Tschentscher, J. T. Costello, A. L. Cavalieri, I. Grguras, A. R. Maier, R. Kienberger, J. Bozek, C. Bostedt, S. Schorb, R. Coffee, M. Messerschmidt, C. Roedig, E. Sistrunk, L. F. DiMauro, G. Doumy, K. Ueda, S. Wada, S. Dusterer, A. K. Kazansky, and N. M. Kabachnik, Phys. Rev. Lett. **108**, 063007 (2012).

[30] S. Düsterer, L. Rading, P. Johnsson, A. Rouzée, A. Hundertmark, M. J. J. Vrakking, P. Radcliffe, M. Meyer, A. K. Kazansky, and N. M. Kabachnik, Journal of Physics B: Atomic, Molecular and Optical Physics **46**, 164026 (2013).

[31] T. Mazza, E. Gryzlova, A. Grum-Grzhimailo, A. Kazansky, N. Kabachnik, and M. Meyer, Journal of Electron Spectroscopy and Related Phenomena **204**, Part B, 313 (2015).

[32] C. I. Blaga, F. Catoire, P. Colosimo, G. G. Paulus, H. G. Muller, P. Agostini, and L. F. DiMauro, Nature Physics **5**, 335 (2009).

[33] M. Odenweller, N. Takemoto, A. Vredenborg, K. Cole, K. Pahl, J. Titze, L. P. H. Schmidt, T. Jahnke, R. Dörner, and A. Becker, Phys. Rev. Lett. **107**, 143004 (2011).

[34] M. Bashkansky, P. H. Bucksbaum, and D. W. Schumacher, Phys. Rev. Lett. **60**, 2458 (1988).

[35] E. Yakaboylu, M. Klaiber, and K. Z. Hatsagortsyan, Phys. Rev. A **90**, 012116 (2014).

[36] I. A. Ivanov and K. T. Kim, Phys. Rev. A **92**, 053418 (2015).

[37] M. Lewenstein, P. Balcou, M. Y. Ivanov, A. L'Huillier, and P. B. Corkum, Phys. Rev. A **49**, 2117 (1994).

[38] D. A. Telnov and S.-I. Chu, Phys. Rev. A **61**, 013408 (1999).

[39] C. P. J. Martiny and L. B. Madsen, Phys. Rev. Lett. **97**, 093001 (2006).
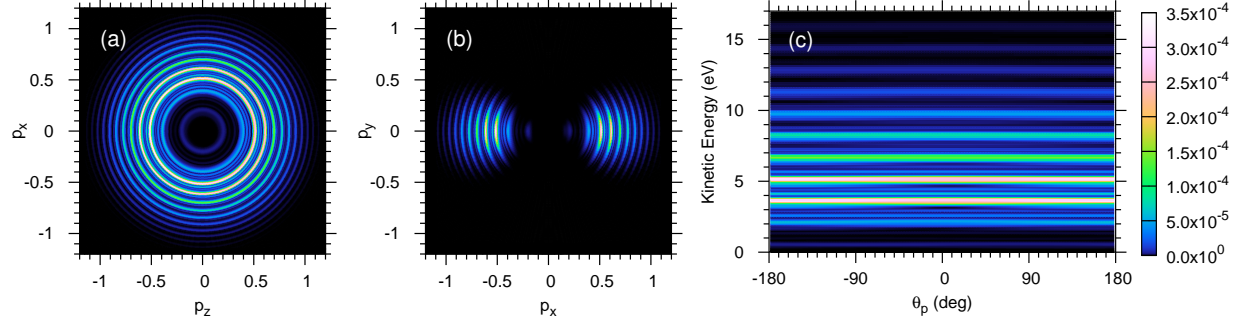
FIG. 1. (Color online) The PMD of the hydrogen atom, driven by the 800nm, 20-cycle circularly polarized laser field ($\varepsilon = 1$, $\alpha = \pi/2$) of peak intensity $I_o = 5 \times 10^{13}$ W/cm^2: (a) cross section of the PMD on the polarization plane ($p_y = 0$), and (b) cross section along the propagation axis ($p_z = 0$) of the driving laser field. (c) The longitudinal PMD in (a) is shown as a function of polar angles θ_p, defined counter-clockwise from the positive p_z-axis on the polarization plane ($y = 0$), and of kinetic energy $(|p_z|^2 + |p_x|^2)/2$ on the polarization plane.
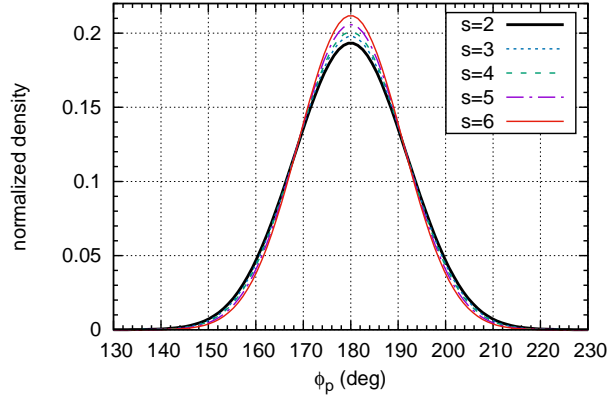
FIG. 2. (Color online) The transversal PMD in FIG. 1(b) at the radius p_s given by Eq. (25) is shown as a function of azimuthal angles ϕ_p, defined counter-clockwise from the positive p_x-axis on the xy-plane (perpendicular to the laser polarization). The electron density for each s (the number of absorbed photons above threshold) is normalized between $\phi_p = 90$ and 270 degrees.
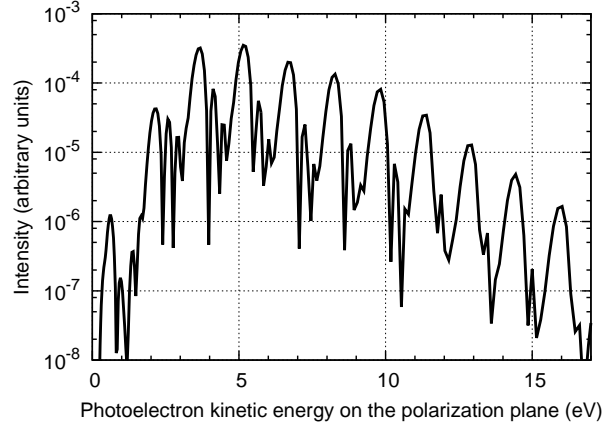
16

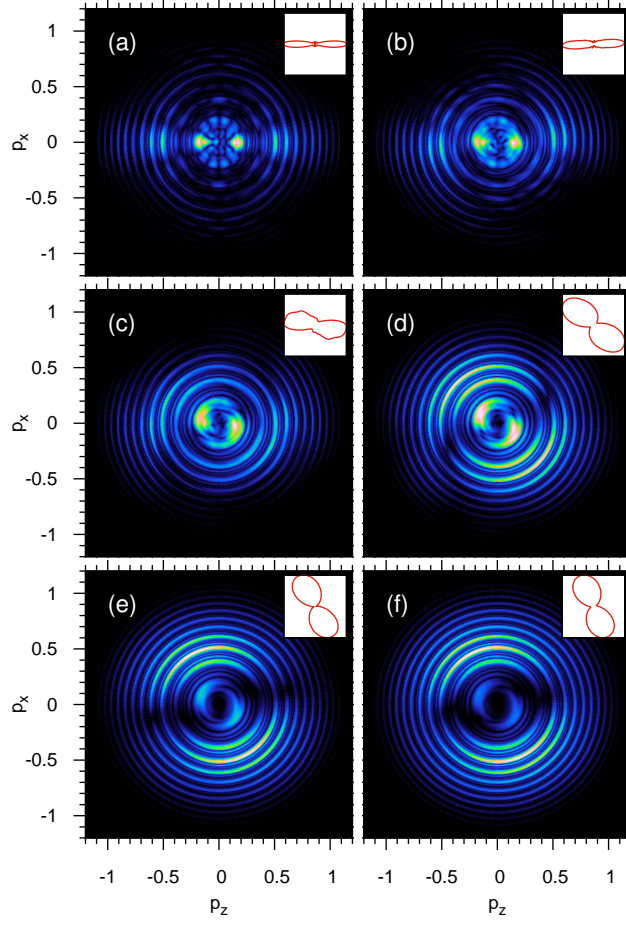FIG. 3. The longitudinal PMD in FIG. 1(c) is integrated over θ_p and shown in the logarithmic scale.

FIG. 4. (Color online) The longitudinal PMD of the hydrogen atom driven by the 800nm, 20-cycle laser field ($\alpha = \pi/2$) of peak intensity $I_o = 5 \times 10^{13}$ W/cm^2 with various ellipticity: (a) $\varepsilon = 0$ (linear polarization), (b) $\varepsilon = 0.2$, (c) $\varepsilon = 0.4$, (d) $\varepsilon = 0.6$, (e) $\varepsilon = 0.8$, and (f) $\varepsilon = 0.87$. Inset figures are the radially integrated and normalized density distributions. Color scales are given in the corresponding figures in FIG. 5.
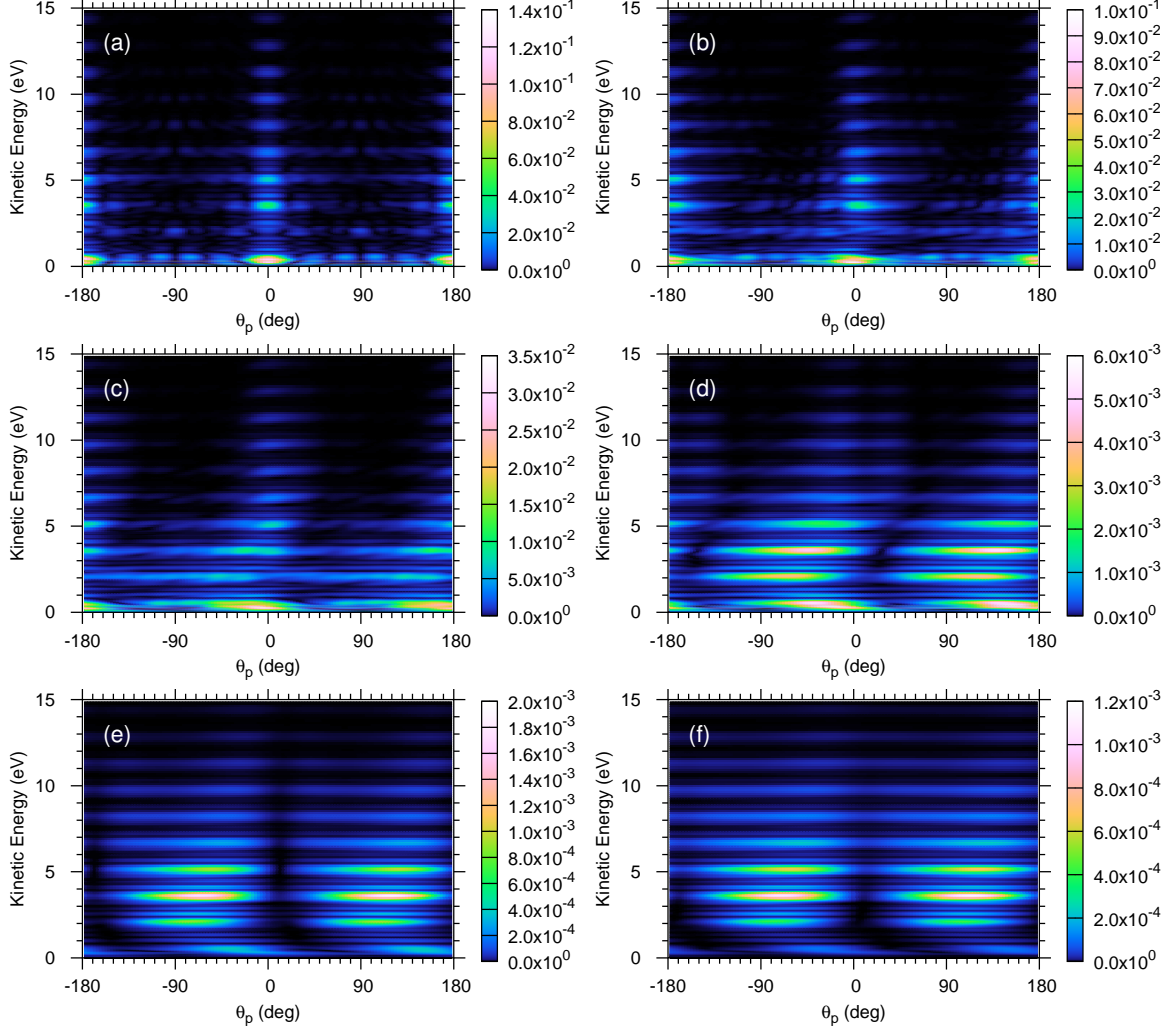
FIG. 5. (Color online) The longitudinal PMDs in FIG. 4 are shown as a function of polar angle θ_p, defined counter-clockwise from the positive p_z-axis, and of kinetic energy on the polarization plane ($y = 0$): (a) $\varepsilon = 0$ (linear polarization), (b) $\varepsilon = 0.2$, (c) $\varepsilon = 0.4$, (d) $\varepsilon = 0.6$, (e) $\varepsilon = 0.8$, and (f) $\varepsilon = 0.87$.
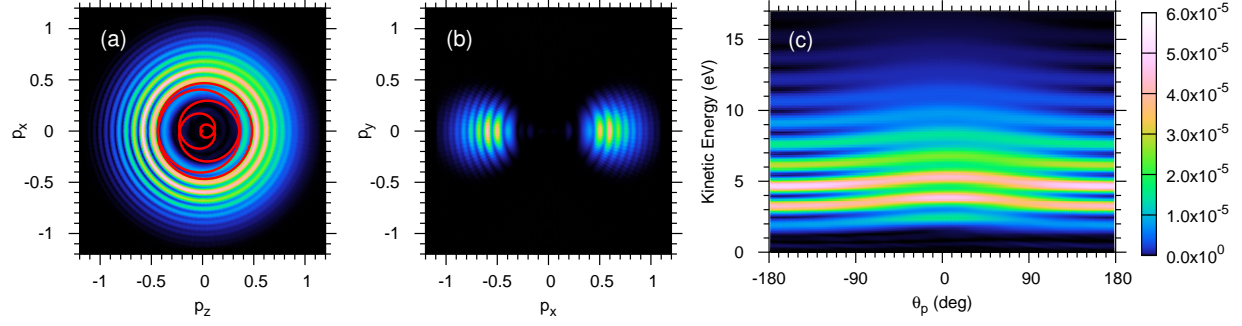
FIG. 6. (Color online) The same as FIG. 1, but the duration of driving laser pulse is reduced to 6 optical cycles. The classical limit of the electron momentum $-\mathbf{A}(t)$ is shown as a solid red line in (a).
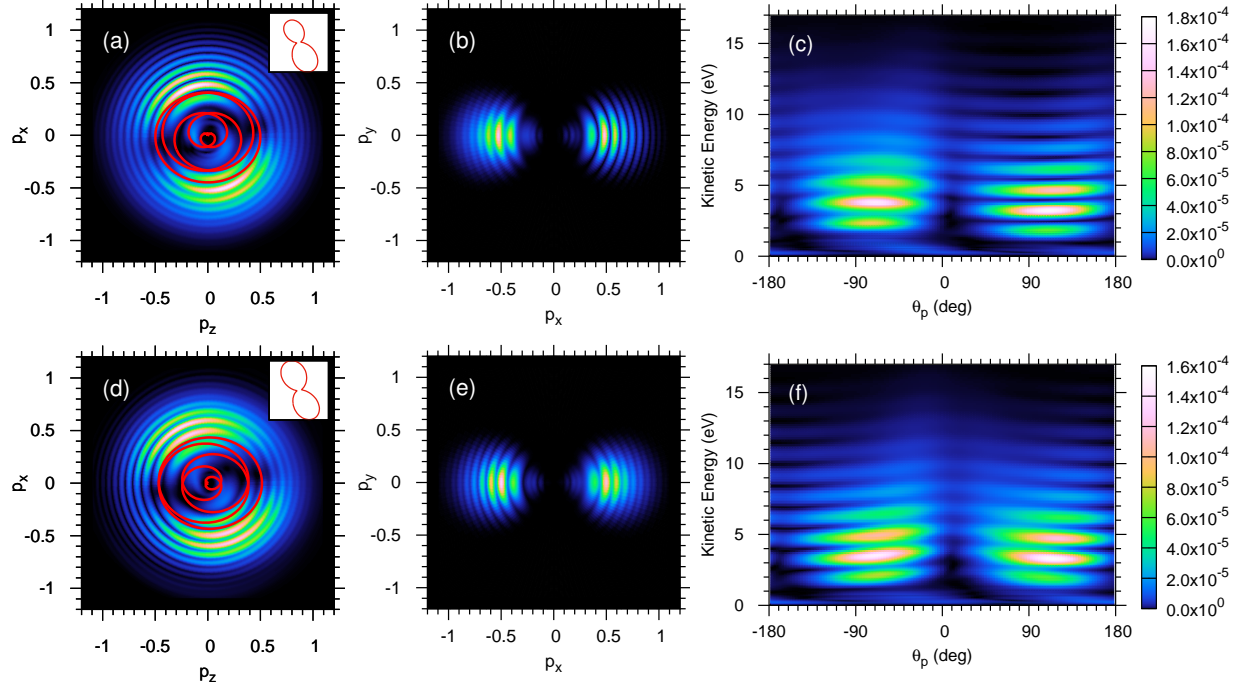

FIG. 7. (Color online) The same as FIG. 6, but with the ellipticity $\varepsilon = 0.87$ and two different CEPs: $\alpha = 0$ (top row), and $\alpha = \pi/2$ (bottom row). Inset figures in (a) and (d) show the radially integrated and normalized density distributions.